Sunlight Induced Photo-thermal Synergistic Catalytic CO_2 Conversion via Localized Surface Plasmon Resonance of MoO_{3-x}

Jue Li,[a#] Yinghao Ye,[b#] Liqun Ye,[ad*] Fengyun Su,[a] Zhaoyu Ma,[a] Jindi Huang,[a] Haiquan Xie,[a] Dmitry E. Doronkin,[c] Anna Zimina,[c] Jan-Dierk Grunwaldt,[c] Ying Zhou,[b*]

a. Engineering Technology Research Center of Henan Province for Solar Catalysis, College of Chemistry and Pharmaceutical Engineering, Nanyang Normal University, Nanyang 473061, P. R. China.

b. State Key Laboratory of Oil and Gas Reservoir Geology and Exploitation, School of Materials Science and Engineering, Southwest Petroleum University, Chengdu, 610500, P. R. China.

c. Institute for Chemical Technology and Polymer Chemistry and Institute of Catalysis Research and Technology, Karlsruhe Institute of Technology, 76131 Karlsruhe, Germany.

d. College of Materials and Chemical Engineering, Key Laboratory of Inorganic Nonmetallic Crystalline and Energy Conversion Materials, China Three Gorges University, Yichang 443002, P. R. China.

Corresponding Author

* Prof. Liqun Ye

E-mail: yeliquny@163.com

* Prof. Ying Zhou

E-mail: yzhou@swpu.edu.cn

[#]The authors contributed equally.

Abstract: Photocatalytic conversion of CO_2 to solar fuels is considered an alternative approach for simultaneously mitigating the greenhouse effect and solving energy shortage. The efficient light harvesting and the thermochemical conversion has been a demanding quest in photocatalysis due to the relatively low solar energy utilization efficiency. In this work, oxygen vacancies are induced in MoO_3 for improving photo-thermal CO_2 reduction efficiency by capturing near-infrared (NIR) photons. The localized surface plasmon resonance (LSPR) of MoO_{3-x} triggered by oxygen vacancies endows the effcient capture of NIR photons. Additionally, oxygen vacancies can promote the carrier separation, improve CO_2 adsorption on the defective surface and lower the barrier of CO_2 hydrogenation during the conversion process. As a result, MoO_{3-x} displayed dramatically enhanced photo-thermal synergistic CO_2 reduction under simulated sunlight (UV-Vis-IR) irradiation than that of MoO_3. The amount of CO produced by MoO_{3-x} can reach 10.3 $\mu mol \cdot g^{-1} \cdot h^{-1}$, which is 20 times higher than that of MoO_3 (0.52 $\mu mol \cdot g^{-1} \cdot h^{-1}$). And the CH_4 production of MoO_{3-x} can reach 2.08 $\mu mol \cdot g^{-1} \cdot h^{-1}$, which is 52 times higher than that of MoO_3 (0.04 $\mu mol \cdot g^{-1} \cdot h^{-1}$). In-situ FT–IR and theoretical calculation also proved the enhanced activity of MoO_{3-x}. This work highlights the significance of defect engineering for improving the photo-thermal catalytic conversion of CO_2.

Key words: carbon dioxide; MoO_{3-x}; photothermal conversion; solar energy

1 Introduction

In modern society, the extensive consumption of fossil fuels will not only cause a the global energy crisis in future, but also gives rise to the climate change by the large amount of carbon dioxide (CO_2) emission.[1] CO_2 is a primary greenhouse gas, and natural photofixation of CO_2 by plants is far from converting sufficient amounts of CO_2. Therefore, seeking sustainable and green ways to realize the effective conversion of CO_2 is extremely urgent. The photocatalytic conversion of CO_2 to hydrocarbon fuels has been reported as an effective, environmentally friendly route for addressing the potential energy and environment crisis simultaneously.[2,3] It offers advantages over the traditional CO_2 conversion technology, such as thermal catalysis[4] and electrocatalysis,[5-8] which need high energy consumption. However, the relatively low efficiency of photocatalytic CO_2 conversion is obtained based on photoexcitation reactions. Recently, photo-thermal synergistic catalysis combining thermochemical and photochemical conversion appeared as a promising method for improving the efficiency.[9,10] Sunlight can be divided into three parts: ultraviolet (UV) light ($\lambda < 400$ nm), visible (Vis) light (400 nm $< \lambda <$ 800 nm) and infrared (IR) light ($\lambda >$ 800 nm). UV-Vis and IR light can induce photocatalytic and thermocatalytic reactions, respectively. Hence, photo-thermal synergistic catalytic CO_2 conversion can be achieved under full spectrum (UV-Vis-IR). However, there are very few catalysts for sunlight induced photo-thermal synergistic catalysis.

To date, a variety of photocatalysts has been developed. At the same time, most photocatalysts cannot capture IR photons for sunlight induced photo-thermal synergistic catalysis. Therefore, various groups are pursuing advanced photocatalytic materials for IR light response. At present, the IR light response materials are mainly noble metal nanomaterials (such as Ag, Au, Ru)[11-13], few heavily doped oxide semiconductors (such as $W_{18}O_{49}$, WO_{3-x}, MoO_{3-x})[14-17], narrow gap semiconductors (such as CuS,[18] Bi_2S_3,[19] black phosphorus) and nano-carbon materials (such as carbon quantum dots, graphene, carbon nanotubes).[20-23] Among them, heavily doped oxide semiconductor materials were employed for the sunlight induced photo-thermal synergistic catalytic CO_2 conversion. And the reasons are following. (1) They show strong localized surface plasmon resonance (LSPR) phenomena, which can enhance IR light absorption to improve the photo-thermal conversion.[24-26] and

(2) more defect sites, which can enhance the adsorption of substrate molecules. At the same time, defect sites also decrease the CO_2 reduction barrier, thus, enhancing the performance of photocatalytic conversion of CO_2 [27] due to photogenerated electrons that determine the reduction reactions. Inspired by these results, we believe that photocatalysts with LSPR effect and vacancies are desirable for achieving higher photo-thermal CO_2 conversion.[28,29]

Compared to the traditional precious metal and other semiconductor oxide photocatalysts, MoO_3 is a potential candidate as photothermocatalyst owing to its powerful oxidation properties, non-toxicity, low cost and versatility.[30-33] But the defect-free MoO_3 shows low photocatalytic reduction performance due to the limited light harvesting, fast hole-electron recombination and small specific surface area. Here, defect engineering is applied to extend the light adsorption, induce the LSPR effect and large specific surface area. The obtained MoO_{3-x} display high activity for photo-thermal synergistic CO_2 reduction under UV-Vis-IR irradiation. The mechanism is studied experimentally by electrochemical characterization and in-situ FT–IR, and theoretical calculations.

Results and Discussion

Experimental sections are described in **Supporting Material**. **Figure 1a** shows the X-ray diffraction (XRD) patterns of MoO_3 and MoO_{3-x}, which are indexed as the orthorhombic phases of MoO_3 (JCPDS No. 01-076-1003) and MoO_{3-x} (JCPDS No. 01-070-0615), respectively.[28,29] Comparing the (020), (040) and (060) peaks of MoO_3 and MoO_{3-x}, it can be found that MoO_3 exposed more {010} facets. It may result from the calcination under oxygen atmosphere to fill up the defect on {010} facets of MoO_{3-x}. The microstructures of MoO_3 and MoO_{3-x} were further analyzed by scanning electron microscopy (SEM), as shown in **Figure S1**.[29,34,35] MoO_3 forms elongated single crystals (**Figure S1a)** with a length of about 50-60 μm, and the width and thickness is about 5 μm and 300 nm, respectively **(Figure S1c)**. MoO_{3-x} is crystallized as elliptical nanosheets **(Figure S1b)** with a length of about 2 μm, and the width and thickness is about 0.5 um and 20 nm **(Figure S1d)**. It can be seen that the morphology of MoO_3 and MoO_{3-x} nanosheets is extremely different. The MoO_{3-x} nanosheets are much smaller and thinner compared with the MoO_3 nanosheets. **Figure S1d** reveals that MoO_{3-x} crystal aggregates are piled up by several layers of

thin nanosheets compared with single pieces of MoO_3 **(Figure S1a).** Furthermore, the edges of MoO_{3-x} are not flat compared with those of MoO_3. The crystal morphologies of MoO_{3-x} and MoO_3 were studied in more detail by transmission electron microscopy (TEM, **Figure 1b-1e**). **Figure 1c** exhibits clear perpendicular lattice fringes with interplanar spacings of about 0.20 and 0.18 nm, corresponding to the theoretical values of the (100) and (002) atomic planes of tetragonal MoO_3, respectively. The corresponding selected area electron diffraction (SAED) pattern shown in **Figure S2a** reveals a 90° angle between the (002) and (100) planes of MoO_3, suggesting that the exposed crystal face is along the (010) plane. Careful observation of the HRTEM images in **Figure 1e** reveals that the pinstripes are much more disordered than those outside the circle marks. The lattice fringes are discontinuous, and some are distorted indicating the presence of crystallographic defects in MoO_{3-x}. The results are consistent with the XRD measurements. HRTEM images furthermore reveal continuous crystal lattice in MoO_{3-x}. The inter-fringe distances are 0.2 and 0.18 nm, corresponding to the (100) and (002) planes of hexagonal MoO_{3-x}, respectively. The corresponding SAED pattern in **Figure S2b** also reveals a 90° angle between the (002) and (100) planes of MoO_{3-x}, suggesting that the exposed crystal face is along the (010).

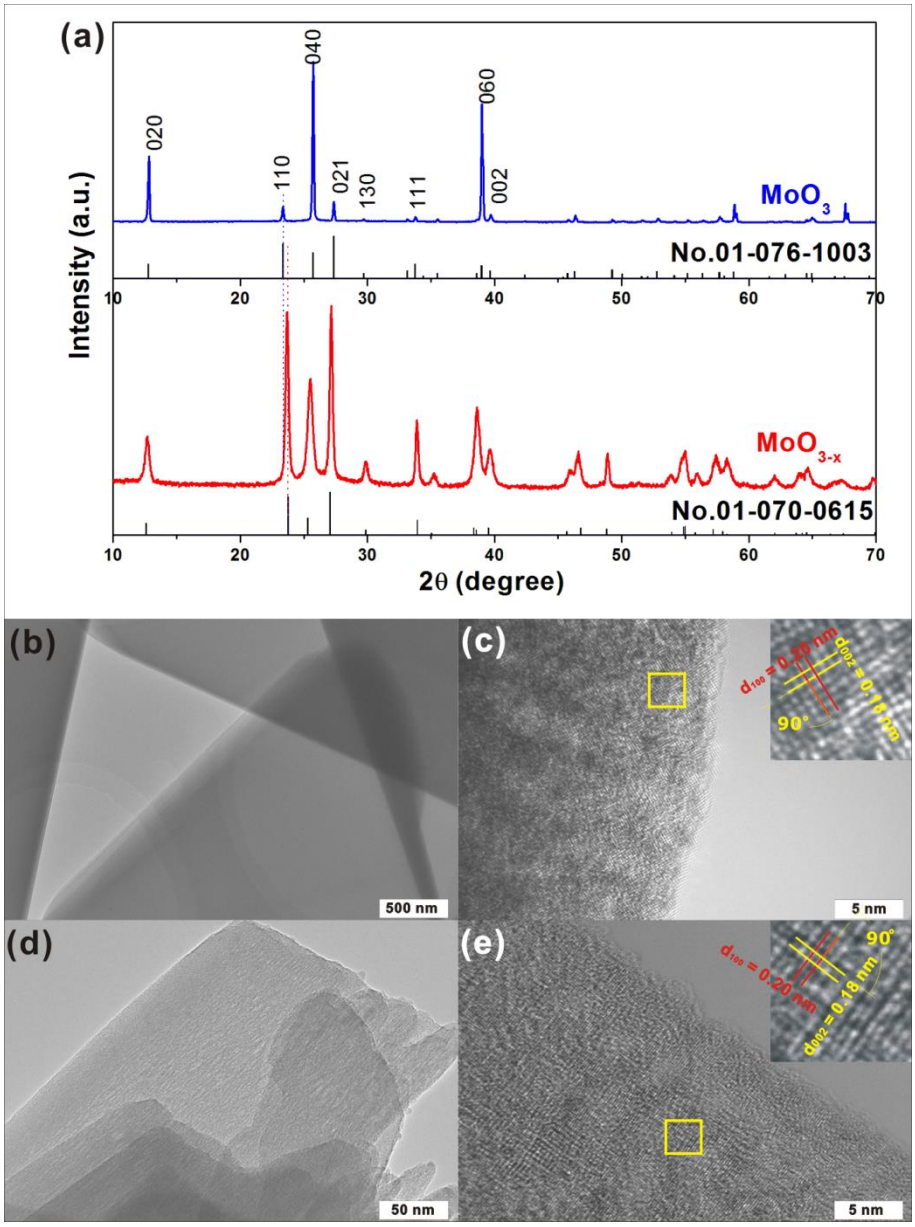

Figure 1. Crystal structure of MoO_{3-x} and MoO_3: (a) XRD patterns, (b) TEM of the MoO_3, (c) TEM of the MoO_{3-x}, (d) HRTEM of the MoO_3 and (e) HRTEM of the MoO_{3-x}.

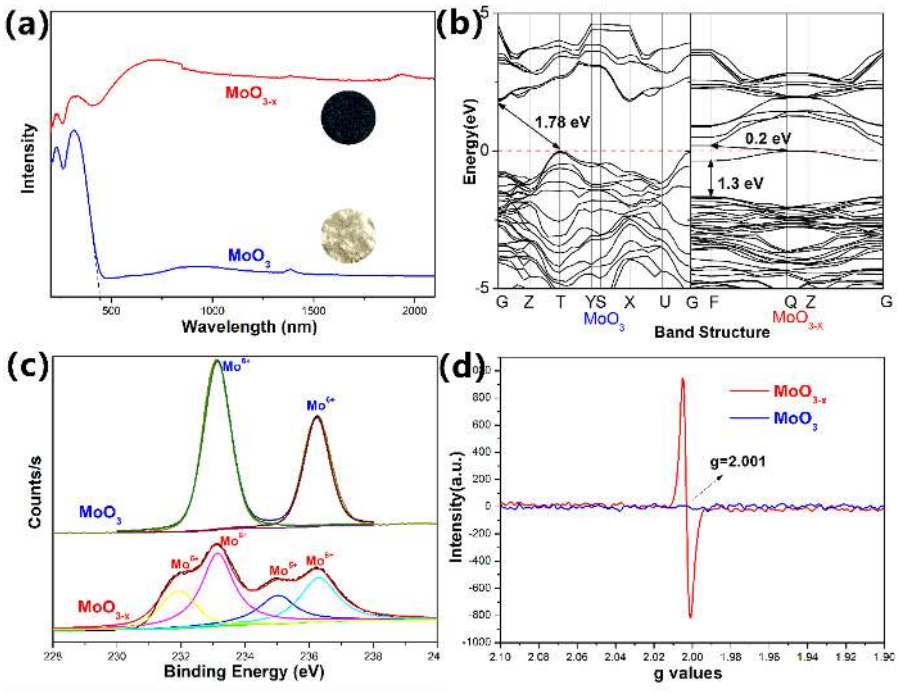

Figure 2. UV-Vis-NIR diffuse reflectance spectra (a), calculated band structure (b), XPS spectra of Mo 3d (c), and ESR spectra (d) of MoO_{3-x} and MoO_3.

Figure 2a shows the UV-Vis-NIR spectra of MoO_{3-x} and MoO_3. The absorption band edge of MoO_3 is at about 443 nm, which corresponds to its wide band gap (ca. 2.80 eV). Thus indicates that MoO_3 can only be excited by UV-Vis light and it may not display sunlight induced photo-thermal synergistic catalytic activity for CO_2 conversion. In contrast, MoO_{3-x} exhibits a strong absorption peak at approximately 700 nm associated with the LSPR of MoO_{3-x} due to the presence of oxygen defects.[28,29] On the other hand, the colors of MoO_{3-x} and MoO_3 are dark blue and pure white, respectively. This also proves that MoO_{3-x} can absorb in the full sunlight spectrum due to the LSPR effect induced by oxygen defects. To understand the oxygen defect-induced LSPR effect, we simulated the energy band structure of MoO_{3-x}. As shown in **Figure 2b**, after the introduction of an oxygen vacancy, the impurity level is generated. And the narrow energy gap results in the full spectrum absorption. Furthermore, from **Figure S3 and S4**, the same phenomenon can be seen in the Density of States (DOS).[36] The oxygen defects change the distribution of HOMO and LUMO. The distribution of HOMO and LUMO on the two layers of MoO_{3-x} restricts the recombination of photo-generated electrons and holes, resulting in the oxygen defect-induced LSPR effect of MoO_{3-x}. The oxygen defect formation was

confirmed by X-ray photoelectron spectroscopy (XPS), electronic spin resonance (ESR), and Raman spectroscopy. **Figure 2c** displays the Mo 3d XPS spectra of MoO_{3-x} and MoO_3. It can be seen that only Mo^{6+} (233.1 eV: $3d_{5/2}$; 236.3 eV: $3d_{3/2}$) exists in MoO_3. In contrast, both Mo^{6+} and Mo^{5+} (231.9 eV: $3d_{5/2}$; 235.0 eV: $3d_{3/2}$) exist in MoO_{3-x}. According to the XPS peak area, Mo^{5+} and Mo^{6+} were about 35% and 65% for total Mo states in the MoO_{3-x}, respectively. The average oxidation state of Mo is thus determined to be mixed-valence state at 5.65, which implies the existence of oxygen defects.[29] The O1s XPS peak shift also implies the existence of oxygen defects. As shown in **Figure S5**, the lower binding energy of MoO_{3-x} (530.7 eV) compared with that of MoO_3 (531.0 eV) indicates different chemical environments. For MoO_{3-x}, there is a new peak at higher binding energy of 532.0 eV, which is caused by surface adsorbed oxygen species.[36,37] This implies that MoO_{3-x} provides many defects for the adsorption of oxygen species. **Figure 2d** shows the ESR spectra of MoO_3 and MoO_{3-x}. MoO_{3-x} exhibits an ESR peak at g = 2.001, which is a typical signal of oxygen defects and is absent in the MoO_3 spectrum.[37] This proves that MoO_3 forms perfect crystals without oxygen defects, which is consistent with previous results. In addition, the Raman spectrum (**Figure S6**) also provides evidence of oxygen defects. Compared with MoO_3, the peak intensity of MoO_{3-x} is significantly reduced, and some peaks are merged or even absent, demonstrating the existence of oxygen vacancies in MoO_{3-x}.[30,38,39]

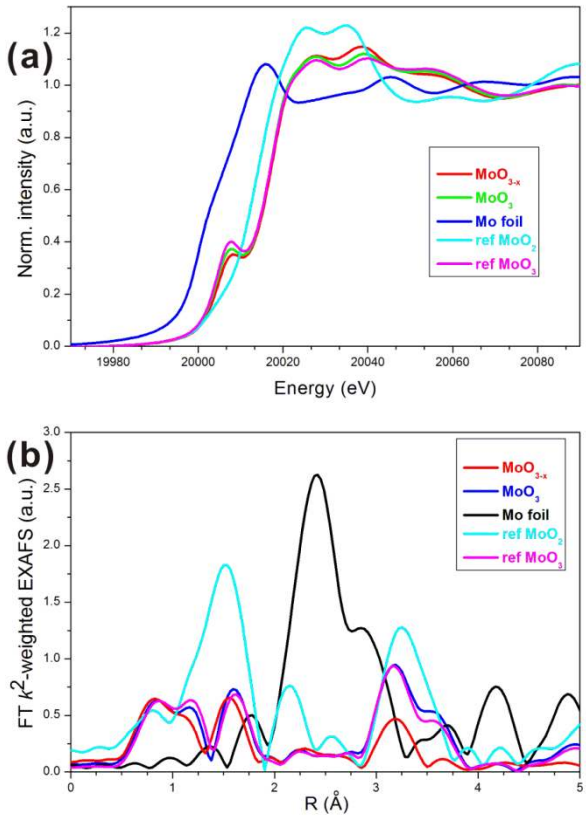

Figure 3. (a) XANES and (b) Fourier-transformed (FT) k^2-weighted EXAFS spectra (uncorrected for the phase shift) of the MoO_{3-x} and MoO_3 with the commercial Mo, MoO_2 and MoO_3 reference spectra.

For directly proving the presence of oxygen defects, X-ray absorption spectra in terms of X-ray Absorption Near Edge Structure (XANES) and Extended X-ray Absorption Fine Structure (EXAFS) are showed in **Figure 3**. The XANES spectrum of the MoO_{3-x} sample is very similar to MoO_3 and commercial MoO_3 reference spectra suggesting the same structure. However, these spectra exhibit two main differences. First, the intensity of the pre-edge at approx. 20007 eV is decreased. This pre-edge is assigned to 1s→4d electronic transition in systems with tetragonal symmetry such as MoO_3 (it is not observed in MoO_2, in which Mo is coordinated by regular octahedrons).[40] The decrease in the pre-edge intensity could result from a partial loss of tetrahedral symmetry due to oxygen defects formation but also due to higher disorder/partial amorphisation of in MoO_{3-x}.[40] The second difference between the MoO_{3-x} and commercial MoO_3 XANES spectra is the shift of the second peak after the absorption maximum (at approx. 20040 eV) to lower energy. Previously, a spectrum with a similar shift and the decreased pre-edge intensity was attributed to Mo_4O_{11}

phase.[41] Quantification of the average oxidation state is possible using the precise position of the second peak after the absorption edge.[42] This yields a stoichiometry of approximately $MoO_{2.7}$, which is consistent with the formation of the Mo_4O_{11} phase, as mentioned earlier. Fourier transformed EXAFS (**Figure 3b**) shows somewhat lower backscattering at r = 1.2 Å not corrected for phase shift which may be attributed to lower average number of oxygen neighbors in the first coordination shell and much lower scattering by the further shells (r between 3 and 4 Å), this is due to the small particle size (nanocrystalline nature) of the MoO_{3-x}. In summary, the material consists of nanocrystalline MoO_{3-x} with high amount of oxygen defects.

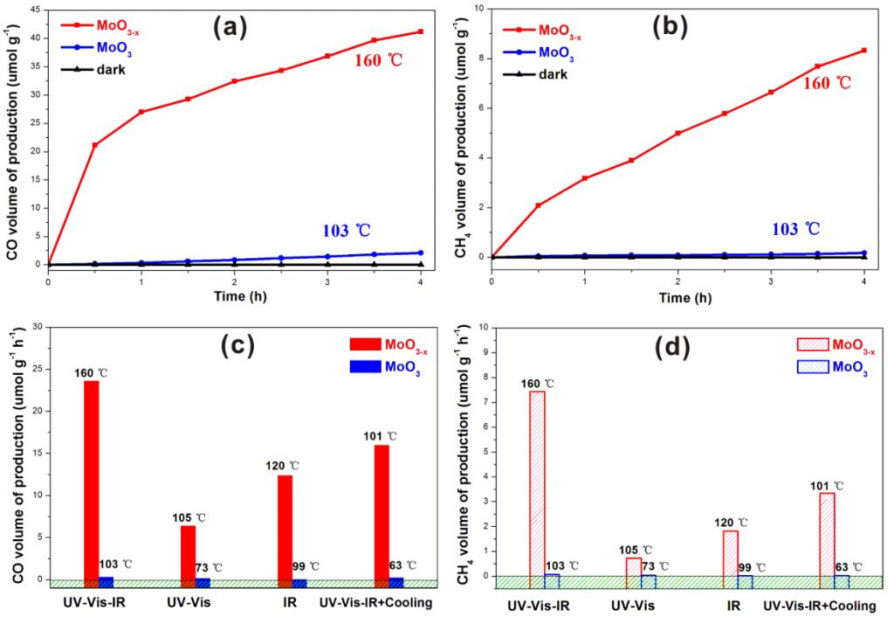

Figure 4. Catalytic CO (a) and CH_4 (b) generation over MoO_{3-x} and MoO_3 under UV-vis-IR light irradiation for 4 h; Rates comparison of CO (c) and CH_4 (d) conversion over MoO_{3-x} and MoO_3 under UV-Vis-IR, UV-Vis, and IR light irradiation for 1 h.

The introduction of oxygen vacancies triggers the LSPR phenomenon of MoO_{3-x}, which darkens the color of the material and extends the light absorption range to the infrared region. Therefore, MoO_{3-x} may display sunlight induced photo-thermal synergistic catalytic activity for CO_2 conversion. As shown in **Figures 4a** and **4b,** it can be clearly seen that MoO_3 and MoO_{3-x} have no catalytic activity without light irradiation. After 4 h UV-Vis-IR light illumination, the amount of CO produced by MoO_{3-x} can reach 41.2 μmol • g^{-1}, which is 20 times higher than that of MoO_3 (2.1 μmol·g^{-1}). And the CH_4 production of MoO_{3-x} can reach 8.3 μmol·g^{-1}, which is 49

times higher than that of MoO_3 (0.17 μmol·g^{-1}). The catalytic results indicate that the introduction of oxygen defects greatly improves the catalytic performance for CO_2 reduction to CO and CH_4. In order to better study the sunlight induced photo-thermal synergistic catalytic CO_2 conversion over MoO_{3-x}, the photocatalytic properties of different wavelength ranges of sunlight were studied. **Figure 4c,d** shows the CO and CH_4 production rates for illumination with UV-Vis-IR, UV-Vis, IR, and UV-Vis-IR light with cooling. Upon illumination with light of all these wavelength ranges, MoO_3 showed negligible activities. In contrast, MoO_{3-x} displayed significant activities for CO_2 reduction to CO and CH_4 upon light illumination in all these wavelength ranges. Comparing the different light wavelength ranges, it can be found that the order of light induced activity of CO and CH_4 production is UV-Vis-IR > IR > UV-Vis. Obviously, this order is follows the temperature order (UV-Vis-IR (160 °C) > IR (120 °C) > UV-Vis (105 °C)). And this order of light induced activity is consistent with that of thermal catalysis (**Figure S7**). It implies that thermal catalysis is very important for CO_2 reduction. In order to confirm it, we used different wavelength LED light sources which did not cause heating (**Figure S8**). It can be seen that the catalytic performance is significantly reduced, which also proves the significance of thermal catalysis induced by light. On the other hand, it also found that the activity of low temperature (101 °C) CO_2 reduction with UV-Vis-IR light irradiation is higher than that of IR (120 °C) light. And UV-Vis-IR induced activity (160 °C) is also higher than the thermal catalytic activity at same temperature of 160 °C. This indicates that thermal catalysis is not the sole cause for the improved activity of MoO_{3-x}, and photocatalys also plays an important role for CO_2 conversion. Based on the above catalytic results, we can summarize that MoO_{3-x} showed sunlight induced photo-thermal synergistic catalytic performance for CO_2 conversion. In addition, the sunlight induced photo-thermal synergistic catalytic activity in CO_2 conversion is also affected by the concentration of oxygen vacancies. As shown in **Figures S9** and **S10**, higher number of oxygen vacancies results in higher activity of MoO_{3-x}.

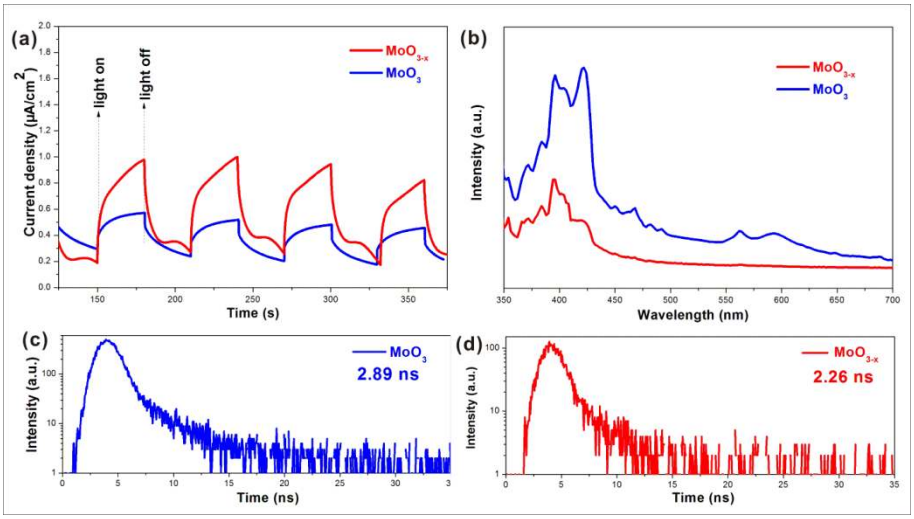

Figure 5. (a) Photocurrent responses, (b) PL spectra, of the MoO_{3-x} and MoO_3, (c) and (d) time-resolved PL spectra of the MoO_3 and MoO_{3-x}.

Photocurrent response, steady-state and transient photoluminescence (PL) spectra and time-resolved PL were investigated to analyze the separation and transfer of photo-generated electrons and holes in the MoO_{3-x} and MoO_3 samples. As shown in **Figure 5a**, the photocurrent response was detected when the light is on, and the photocurrent density of MoO_{3-x} is about two times higher than that of MoO_3. It confirms the high separation efficiency of photo-induced electron-hole pairs for MoO_{3-x}. The photoluminescence spectra of the MoO_{3-x} and MoO_3 are shown in **Figure 5b**. The main emission peaks are observed at 396 and 422 nm, which are intrinsic excitation of MoO_3 and MoO_{3-x}, respectively. Compared to MoO_3, the emission intensity of the MoO_{3-x} decreased after introduction of oxygen vacancies.[33] In addition, the kinetics of charge separation in the photocatalysts was detected with time-resolved fluorescence decay spectra as shown in **Figures 5c and 5d**. The lifetimes (τ) were 2.89 ns (MoO_3) and 2.26 ns (MoO_{3-x}), indicating that the photogenerated carriers of MoO_{3-x} are more rapidly separates, and thus, are able to drive redox reactions.[43,44] They further confirm that oxygen defects promote interfacial charge transfer, separation and migration of photo-induced charge carriers. On the other hand, oxygen defects also elevate the conduction band (CB) position, which is useful for photocatalytic CO_2 reduction reaction. As shown in **Figure S11**, the VB-XPS spectrum shows that the VB position of MoO_3 and MoO_{3-x} are 3.23 and 0.23 eV, respectively. Because of the same intrinsic band gap of 2.8 eV, the CB position of MoO_3 and MoO_{3-x} are 0.43 and -2.57 eV, respectively. This may be at the origin that

MoO_{3-x} displayed higher activity than MoO_3 for CO_2 reduction.

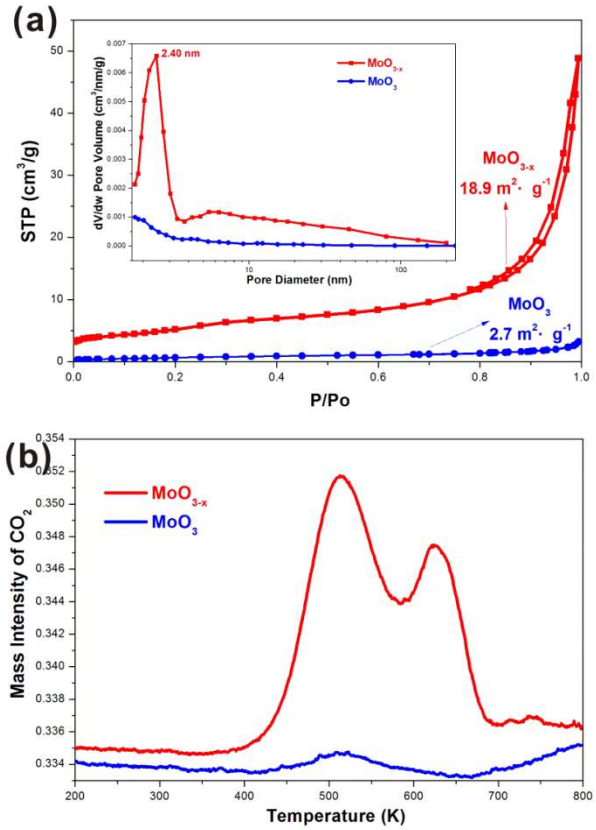

Figure 6 (a) BET and corresponding pore size distribution curves, and (b) TPD of CO_2 from MoO_{3-x} and MoO_3.

For heterogeneous gas-solid carbon dioxide conversion reaction, the adsorption properties of the material greatly affect the performance. **Figure 6a** shows BET plots and pore size distribution curves of MoO_{3-x} and MoO_3, revealing that the specific surface area of MoO_{3-x} is larger than that of MoO_3. Based on the type of hysteresis loop, the pores of MnO_{3-x} should be wedge-shaped. In addition, the pore size distribution of MoO_{3-x} has a mean value of 2.4 nm with a mean pore volume of 0.073 $cm^3\ g^{-1}$. In contrast, MoO_3 showed ultra-low specific surface area and pore volume. It is also consistent with the foregoing morphology analysis. **Figure S12** shows the adsorption of CO_2 on the two materials, revealing that the amount of CO_2 adsorbed on MoO_{3-x} is larger than on MoO_3. **Figure 6b** shows the CO_2 temperature programmed desorption (TPD) of MoO_{3-x} and MoO_3. Two strong peaks at 513 and 625 °C are found in MoO_{3-x} while only one weak peak at 513 °C appears in the TPD profile of MoO_3. It indicates that MoO_{3-x} can adsorb more CO_2 molecules, and the adsorption strength is also stronger than MoO_3, which is better associated with

BET.[45,46] Therefore, MoO_{3-x} displays better catalytic activity for CO_2 reduction. After normalization by specific surface area, the activity of MoO_{3-x} (0.55 $\mu mol \cdot m^{-2} \cdot h^{-1}$) is still greater than MoO_3 (0.19 $\mu mol \cdot m^{-2} \cdot h^{-1}$), indicating that the specific surface area is only one of the factors affecting the reduction performance of carbon dioxide.

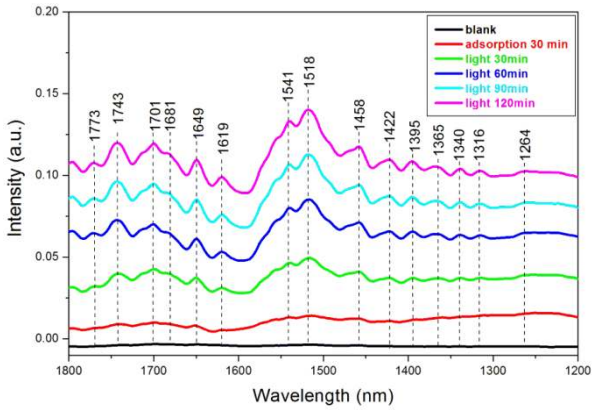

Figure 7 In-situ FT–IR spectra of the reaction of CO_2 and H_2O on MoO_{3-x}: (1) without CO_2 gas and irradiation; (2) with flowing CO_2 gas for 30 min without irradiation; and with irradiation for (3) 30 min, (4) 60 min, (5) 90 min, and (6) 120 min.

In-situ FT–IR measurements on MoO_{3-x} were carried out to study the mechanism of the photocatalytic CO_2 reduction. As shown in **Figure 7**, after introducing water-containing CO_2 gas into the system without light irradiation, no peaks appeared. However, after turning on the light, monodentate carbonate (m–CO_3^{2-}; 1316, 1340, 1458, and 1518 cm^{-1}), bidentate carbonate (b–CO_3^{2-}; 1264, and 1541 cm^{-1}), polydentate carbonate (p–CO_3^{2-}; 1395 cm^{-1}), carboxylate (CO_2^-; 1681 cm^{-1}), bicarbonate (HCO_3^-; 1422 and 1649 cm^{-1}), formate (1385, 1619, and 1743 cm^{-1}) and surface formic acid (HCOOH, at 1701 cm^{-1}) appeared.[47–51] And with prolonged light illumination all peaks gained intensity. It illustrates that CO_2 molecules were firstly adsorbed on the surface of MoO_{3-x} composite. And then the light induced the enhancement of CO_2 adsorption. At end, CO_2 molecules were transformed into various intermediate products.

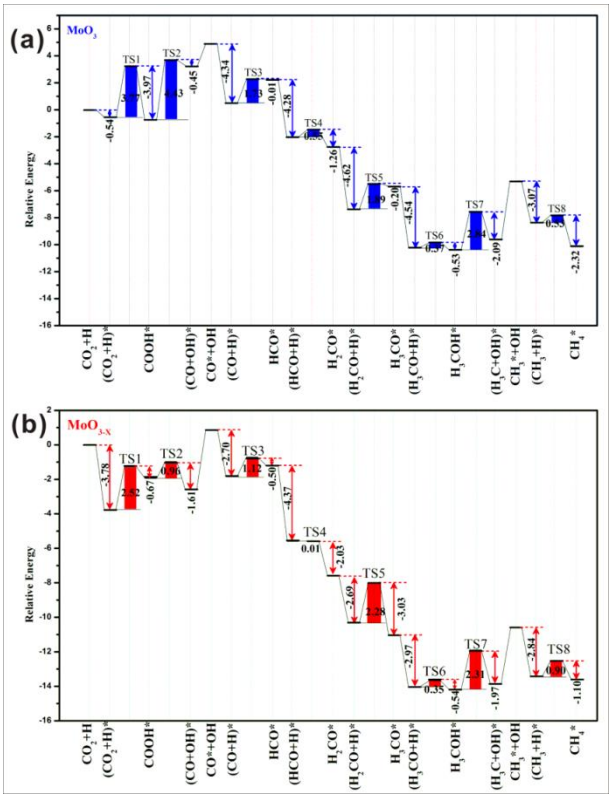

Figure 8 Reaction pathways for CO_2 reduction to CO and CH_4 on (a) MoO_3 and (b) MoO_{3-x} surfaces.

In order to gain deeper understanding of the mechanism of CO_2 reduction on MoO_3 and MoO_{3-x} catalysts, DFT calculations were carried out. All details of the CO_2 reduction pathways to CO and CH_4 on the MoO_3 and MoO_{3-x} surfaces are shown in **Figure 8**. The reaction includes an eight-electron transfer process, and the most stable product in each of these steps could be clearly identified. The initial step of CO_2 hydrogenation reduction is formation the COOH*. Subsequently, the CO, HCO, H_2CO, H_3CO, H_3COH and CH_4 are formed from COOH*. Meanwhile, structures of all calculated intermediates in CO_2 reduction on the MoO_3 and MoO_{3-x} surfaces are shown in **Figure S13 and S14**. The energy barriers of CO_2 hydrogenation reduction to COOH are 3.77 and 2.52 eV on the MoO_3 and MoO_{3-x} surfaces, respectively, while the COOH dissociation is 4.43 and 0.97 eV. Meanwhile, the energy of barriers on the MoO_3 and MoO_{3-x} surface are, respectively: 1.74 and 0.98 eV of CO hydrogenation, 0.55 and 0.04 eV of HCO hydrogenation, 1.89 and 2.28 eV of H_2CO hydrogenation, 0.37 and 0.35 eV of H_3CO hydrogenation, 2.84 and 2.31 eV of H_3COH dehydroxylation and 0.53 and 0.90 eV of CH_3 hydrogenation. As shown in the **Figure 8,** MoO_{3-x} has a lower barrier than MoO_3 for the CO_2 reduction to CH_4. Therefore, MoO_{3-x} showed the

enhanced activity for sunlight induced photo-thermal synergistic catalytic CO_2 conversion.

Conclusions

Oxygen-deficient MoO_{3-x} has been successfully synthesized in this work. The LSPR effect induced by oxygen vacancies has narrowed the band gap of MoO_3 and extended the absorption range to the infrared region. The IR absorption endows strong thermal effect in MoO_{3-x} and larger specific surface area provides more active sites. Besides, the introduction of oxygen vacancies decreased the barrier for CO_2 hydrogenation and recombination of photogenerated electrons and holes. Finally, effective photothermal CO_2 conversion efficiency under UV-Vis-IR light is obtained on MoO_{3-x}. This present study proves that introducing oxygen vacancies is a feasible approach for achieving highly efficient UV-Vis-IR driven photo-thermal catalysts.

Acknowledgments

This work was supported by the National Natural Science Foundation of China (No. 51872147, 21671113), the 111 Project of Hubei Province (2018-19), and the Program for Innovative Research Team of Science and Technology in the University of Henan Province (19IRTSTHN025). We also thank Synchrotron Radiation Source at KIT, Karlsruhe for providing beamtime and Dr. Tim Pruessmann at CAT-ACT for the support during measurements.

References

[1] R. M. Duren, C. E. Miller, Measuring the carbon emissions of megacities, Nature Climate Change, 2012, 2, 560-562.

[2] K. W. Anthony, T. S. v. Deimling, I. Nitze, S. Frolking, A. Emond, R. Daanen, P. Anthony, P. Lindgren, B. Jones, G. Grosse, 21st-century modeled permafrost carbon emissions accelerated by abrupt thaw beneath lakes, Nat. Commun., 2018, 9, 3262.

[3] X. Lim, How to make the most of carbon dioxide, Nature, 2015, 526, 628-630.

[4] P. V. Kumar, N. M. Bardhan, G. Y. Chen, Z. Li, A. M. Belcher, J. C. Grossman, New insights into the thermal reduction of graphene oxide: Impact of oxygen clustering, Carbon, 2016, 100, 90-98.

[5] S. Lee, J. Lee, Electrode Build-Up of Reducible Metal Composites toward Achievable Electrochemical Conversion of Carbon Dioxide, Chem Sus Chem, 2016, 9, 333-344.

[6] S. Schlager, A. Fuchsbauer, M. Haberbauer, H. Neugebauera, N. S. Sariciftci, Carbon dioxide conversion to synthetic fuels using biocatalytic electrodes, J. Mater. Chem. A, 2017, 5, 2429-2443.

[7] W. Li, M. Seredych, E. Rodríguezcastellón, T. J. Bandosz, Metal-free Nanoporous Carbon as a Catalyst for Electrochemical Reduction of CO_2 to CO and CH_4, Chem Sus Chem, 2016, 9, 606-616.

[8] R. Kortlever, J. Shen, Klaas J. P. Schouten, F. Calle-Vallejo, M. T. M. Koper, Catalysts and Reaction Pathways for the Electrochemical Reduction of Carbon Dioxide, J. Phys. Chem. Lett., 2015, 6, 4073-4082.

[9] Y. Bai, P. Yang, P. Wang, H. Xie, H. Dang, L. Ye, Semimetal bismuth mediated UV–vis-IR driven photo-thermocatalysis of $Bi_4O_5I_2$ for carbon dioxide to chemical energy, J. CO_2 Utili., 2018, 23, 51-60.

[10] L. Zhi, H. Zhang, Z. Yang, W. Liu, B. Wang, Interface coassembly of mesoporous MoS_2 based-frameworks for enhanced near-infrared light driven photocatalysis, Chem. Commun., 2016, 52, 6431-6434.

[11] K. Takemuraa, O. Adegokeb, N. Takahashia, T. Katob, T. C. Lid, Noritoshi Kitamotoe, Tomoyuki Tanakaf, Tetsuro Suzukig, Enoch Y. Park, Versatility of a localized surface plasmon resonance-based gold nanoparticle-alloyed quantum dot nanobiosensor for immunofluorescence detection of viruses, Biosensors Bioelectronics, 2016, 89, 998-1005.

[12] Z. Yin, Y. Wang, C. Song, L. Zheng, N. Ma, X. Liu, S. Li, L. Lin, M. Li, Y. Xu, W. Li, G. Hu, Z. Fang, D. Ma, Hybrid Au−Ag Nanostructures for Enhanced Plasmon-Driven Catalytic Selective Hydrogenation through Visible Light Irradiation and Surface-Enhanced Raman Scattering, J. Am. Chem. Soc., 2018, 140, 864-867.

[13] X. Cai, M. Zhu, O. A. Elbanna, M. Fujitsuka, S. Kim, L. Mao, J. Zhang, T. Majima, Au Nanorod Photosensitized $La_2Ti_2O_7$ Nanosteps: Successive Surface Heterojunctions Boosting Visible to Near-Infrared Photocatalytic H_2 Evolution, ACS Catal., 2018, 8, 122-131.

[14] L. Liang, X. Li, Y. Sun, Y. Tan, X. Jiao, H. Ju, Z. Qi, J. Zhu, Y. Xie, Infrared Light-Driven CO_2 Overall Splitting at Room Temperature, Joule, 2018, 2, 1004-1016.

[15] L. Wang, Y. Wang, Y. Cheng, Z. Liu, Q. Guo, M. N. Ha, Z. Zhao, Hydrogen-treated mesoporous WO_3 as a reducing agent of CO_2 to fuels (CH_4 and CH_3OH) with

enhanced photothermal catalytic performanc, J. Mater. Chem. A, 2016, 4, 5314-5322.
[16] Y. Kuwahara, Y. Yoshimura, K. Haematsu, H. Yamashita, Mild Deoxygenation of Sulfoxides over Plasmonic Molybdenum Oxide Hybrid with Dramatic Activity Enhancement under Visible Light, J. Am. Chem. Soc., 2018, 140, 9203−9210.
[17] H. S. Kim, J. B. Cook, H. Lin, J. S. Ko, S. H. Tolbert, V. Ozolins, B. Dunn, Oxygen vacancies enhance pseudocapacitive charge storage properties of MoO_{3-x}, Nat. Mater, 2017, 16, 454-460.
[18] D. Zhou, D. Liu, W. Xu, Z. Yin, X. Chen, P. Zhou, S. Cui, Z. Chen, H. Song, Enhancement Induced by $Cu_{2-x}S$ Plasmon Nanoparticles, ACS Nano., 2016, 10, 5169-5179.
[19] G. Chen, Y. Yu, K. Zheng, T. Ding, W. Wang, Y. Jiang, Q. Yang, Fabrication of ultrathin Bi_2S_3 nanosheets for high-performance, flexible, visible–NIR photodetectors, Small, 2015, 11, 2848-2855.
[20] Y. Du, S. Guo, Chemically doped fluorescent carbon and graphene quantum dots for bioimaging, sensor, catalytic and photoelectronic applications, Nanoscale, 2016, 8, 2532-2543.
[21] Q. Xiang, J. Yu, M. Jaroniec, Graphene-based semiconductor photocatalysts, Chem. Soc. Rev., 2012, 41, 782-796.
[22] J. Liu, Y. Liu, N. Liu, Y. Han, X. Zhang, H. Huang, Y. Lifshitz, S. T. Lee, J. Zhong, Z. Kang, Metal-free efficient photocatalyst for stable visible water splitting via a two-electron pathway, Science, 2015, 347, 970-974.
[23] G. A. M. Hutton, B. C. M. Martindale, E. Reisner, Carbon dots as photosensitisers for solar-driven catalysis, Chem. Soc. Rev., 2017, 46, 6111-6123.
[24] M. M. Rahman, S. H. Im, J. J. Lee, Enhanced photoresponse in dye-sensitized solar cells via localized surface plasmon resonance through highly stable nickel nanoparticles, Nanoscale, 2016, 8, 7769-7769.
[25] S. H. Lee, H. Nishi, T. Tatsuma, Plasmonic behaviour and plasmon-induced charge separation of nanostructured MoO_{3-x} under near infrared irradiation, Nanoscale, 2018, 10, 2841-2847.
[26] C. Li, T. Wang, Z. J. Zhao, W. Yang, J. F. Li, A. Li, Z. Yang, G. A. Ozin, J. Gong, Promoted Fixation of Molecular Nitrogen with Surface Oxygen Vacancies on Plasmon-Enhanced TiO_2 Photoelectrodes, Angew. Chem. 2018, 130, 5376 -5380.

[27] Z. Ma, P. Li, L. Ye, Y. Zhou, F. Su, C. Ding, H. Xie, Y. Bai, P. K. Wong, Oxygen Vacancies Induced Exciton Dissociation of Flexible BiOCl Nanosheets for Effective Photocatalytic CO_2 Conversion, J. Mater. Chem. A., 2017, 5, 24995-25004.

[28] H. Yin, Y. Kuwahara, K. Mori, H. Cheng, M. Wen, H. Yamashita, High-surface-area plasmonic MoO_{3-x}: rational synthesis and enhanced ammonia borane dehydrogenation activity, J. Mater. Chem. A, 2017, 5, 8946-8953.

[29] H. Cheng, T. Kamegawa, K. Mori, H. Yamashita, Surfactant-Free Nonaqueous Synthesis of Plasmonic Molybdenum Oxide Nanosheets with Enhanced Catalytic Activity for Hydrogen Generation from Ammonia Borane under Visible Light, Angew. Chem. Int. Ed., 2014, 53, 2910-2914.

[30] M. M. Y. A. Alsaif, A. F. Chrimes, T. Daeneke, S. Balendhran, D. O. Bellisario, Y. Son, M. R. Field, W. Zhang, H. Nili, E. P. Nguyen, K. Latham, J. V. Embden, M. S. Strano, J. Z. Ou, K. Kalantar-zadeh, High-Performance Field Effect Transistors Using ElectronicInks of 2D Molybdenum Oxide Nanoflakes, Adv. Funct. Mater., 2016, 26, 91-100.

[31] S. Yang, Z. Wang, Y. Hu, X. Luo, J. Lei, D. Zhou, L. Fei, Y. Wang, H. Gu, Highly Responsive Room-Temperature Hydrogen Sensing of α-MoO_3 Nanoribbon Membranes, ACS Appl. Mater. Interfaces, 2015, 7, 9247-9253.

[32] B. Yao, L. Huang, J. Zhang, X. Gao, J. Wu, Y. Cheng, X. Xiao, B. Wang, Y. Li, J. Zhou, Flexible Transparent Molybdenum Trioxide Nanopaper for Energy Storage. Adv. Mater., 2016, 28, 6353-6358.

[33] P. Meduri, E. Clark, J. H. Kim, E. Dayalan, G. U. Sumanasekera, M. K. Sunkara, MoO_{3-x} Nanowire Arrays As Stable and High-Capacity Anodes for Lithium Ion Batteries, Nano Lett., 2012, 12, 1784-1788.

[34] G. Zhang, T. Xiong, M. Yan, L. He, X. Liao, C. He, C. Yin, H. Zhang, L. Mai, α-MoO_{3-x} by plasma etching with improved capacity and stabilized structure for lithium storage, Nano Energy, 2018, 49, 555-563.

[35] A. Pathak, A. S. Gangan, S. Ratha, B. Chakraborty, C. S. Rout, Enhanced Pseudocapacitance of MoO_3‑Reduced Graphene Oxide Hybrids with Insight from Density Functional Theory Investigations, J. Phys. Chem. C, 2017, 121, 18992-19001.

[36] H. Cheng, M. Wen, X. Ma, Y. Kuwahara, K. Mori, Y. Dai, B. Huang, H. Yamashita, Hydrogen Doped Metal Oxide Semiconductors with Exceptional and Tunable Localized Surface Plasmon Resonances, J. Am. Chem. Soc., 2016, 138, 9316−9324.

[37] F. Tian, H. Zhao, G. Li, Z. Dai, Y. Liu, R. Chen, Modification with Metallic Bismuth as Efficient Strategy for the Promotion of Photocatalysis: The Case of Bismuth Phosphate, Chem Sus Chem, 2016, 9, 1579 -1585.

[38] F. Ji, X. Ren, X. Zheng, Y. Liu, L. Pang, J. Jiang, S. Liu, 2D-MoO_3 nanosheets for superior gas sensors, Nanoscale, 2016, 8, 8696-8703.

[39] M. M. Y. A. Alsaif, M. R. Field, T. Daeneke, A. F. Chrimes, W. Zhang, B. J. Carey, K. J. Berean, S. Walia, J. V. Embden, B. Zhang, K. Latham, K. Kalantar-zadeh, J. Z. Ou, Exfoliation Solvent Dependent Plasmon Resonances in Two-Dimensional Sub-Stoichiometric Molybdenum Oxide Nanoflakes, ACS Appl. Mater. Interfaces, 2016, 8, 3482-3493.

[40] T. Ressler, O. Timpe, T. Neisius, J. Find, G. Mestl, M. Dieterle, R. Schlögl, Time-Resolved XAS Investigation of the Reduction/Oxidation of MoO_{3-x}, J. Catal., 2000, 191, 75-85.

[41] T. Ressler, R. E. Jentoft, J. Wienold, M. M. Günter, and O. Timpe, In Situ XAS and XRD Studies on the Formation of Mo Suboxides during Reduction of MoO_3, J. Phys. Chem. B, 2000, 104 (27), 6360–6370.

[42] T. Ressler, J. Wienold, R. E. Jentoft, T. Neisius, Bulk Structural Investigation of the Reduction of MoO_3 with Propene and the Oxidation of MoO_2 with Oxygen, J. Catal, 2002, 210, 67-83.

[43] Y. Li, H. Xu, S. Ouyang, D. Lu, X. Wang, D. Wang, J. Ye, In situ surface alkalinized g-C_3N_4 toward enhancement of photocatalytic H_2 evolution under visible-light irradiation, J. Mater. Chem. A, 2016, 4, 2943-2950.

[44] N. Tian, Y. Zhang, X. Li, K. Xiao, X. Du, F. Dong, G. I. N. Waterhouse, T. Zhang, H. Huang, Precursor-reforming protocol to 3D mesoporous g-C_3N_4 established by ultrathin self-doped nanosheets for superior hydrogen evolution, Nano Energy, 2017, 38, 72-81.

[45] G. Liu, Q. Zhang, Y. Han, N. Tsubakia, Y. Tan, Effects of the MoO_3 structure of Mo-Sn catalysts on dimethyl ether oxidation to methyl formate under mild conditions, Green Chem., 2015, 17, 1057-1064.

[46] D. V. N. Vo, A. A. Adesina, A potassium-promoted Mo carbide catalyst system for hydrocarbon synthesis, Catal. Sci. Technol., 2012, 2, 2066-2076.

[47] J. Ran, W. Guo, H. Wang, B. Zhu, J. Yu, S. Qiao, Metal-Free 2D/2D

phosphorene/g-C_3N_4 van der Waals heterojunction for highly enhanced visible-light photocatalytic H_2 production, Adv. Mater. 2018, 30, 1800128.

[48] T. Di, B. Zhu, B. Cheng, J. Yu, J. Xu, A direct Z-scheme g-C_3N_4/SnS_2 photocatalyst with superior visible-light CO_2 reduction performance, J. Catal., 2017, 352, 532-541.

[49] S. Cao, Y. Li, B. Zhu, M. Jaroniec, J. Yu, Facet effect of Pd co-catalyst on photocatalytic CO_2 reduction over g-C_3N_4, J. Catal., 2017, 349, 208-217.

[50] P. Xia, B. Zhu, J. Yu, S. Cao, M. Jaronie, Ultra-thin nanosheet assemblies of graphitic carbon nitride for enhanced photocatalytic CO_2 reduction, J. Mater. Chem. A, 2017, 5, 3230–3238.

[51] J. Fu, B. Zhu, C. Jiang, B. Cheng, W. You, J. Yu, Hierarchical porous O-doped g-C_3N_4 with enhanced photocatalytic CO_2 reduction activity, Small, 2017, 13, 1603938.